Drug Design, Development and Therapy

Dovepress
Taylor & Francis Group

Open Access Full Text Article

ORIGINAL RESEARCH

Celecoxib-Loaded "Nano-in-Nano" Hierarchical Delivery System: Structure-Driven Synergistic Optimization of Diffusion Efficiency and Mechanical Stability for Osteoarthritis Therapy

Chuangzan Yang[1,2], Huashen He[1–3], Yichao Li[1–3], Sa Huang[1–3], Yingneng Zhang[1,2], Weixin Xiao[1–3], Zhixuan Peng[1,2], Xueyuan Luo[1,2], Shuohan Jiang[1,2], Yu Li[1,2], Liran Cen[1,2], Huanhuan Jia[4], Ying Liu[5], Junfeng Ban[1–3]

[1]Guangdong Pharmaceutical University, Guangzhou, People's Republic of China; [2]Engineering Research Center of Small Molecule Drugs Ministry of Education, Guangdong Pharmaceutical University, Guangzhou, People's Republic of China; [3]Guangdong Provincial Key Laboratory of Pharmaceutical Preparations Research and Evaluation, Guangdong Pharmaceutical University, Guangzhou, People's Republic of China; [4]Medical Devices Research & Testing Center, South China University of Technology, Guangzhou, People's Republic of China; [5]Graduate School, Guangdong Pharmaceutical University, Guangzhou, People's Republic of China

Correspondence: Huanhuan Jia, Medical Devices Research & Testing Center, South China University of Technology, Guangzhou, Guangdong, 51006, People's Republic of China, Email jiahuanhuan@scut.edu.cn; Junfeng Ban, School of Pharmacy, Guangdong Pharmaceutical University, Guangzhou, Guangdong, 51006, People's Republic of China, Email banjunfeng@163.com

Purpose: Osteoarthritis (OA) joints present abnormal mechanical environments that limit drug retention and therapeutic efficacy. Current intra-articular systems cannot provide both sustained anti-inflammatory delivery and mechanical support. A celecoxib (CXB)-loaded "Nano-in-Nano" Hierarchical Delivery System (NiN-HDS) was developed to simultaneously optimize drug release and joint reinforcement.

Methods: In this study, celecoxib-loaded PLGA nanoparticles (CXB-NPs) were prepared by emulsion solvent evaporation and incorporated into an electrospun nanofiber membrane combined with a genipin-crosslinked gelatin layer to form NiN-HDS. The system was characterized for particle size, zeta potential, porosity, hydrophilicity, swelling, degradation, mechanical properties, and in vitro CXB release. Therapeutic potential was evaluated in a rat OA model using histological and immunohistochemical analyses of cartilage and inflammatory markers.

Results: NiN-HDS maintained nanoparticle stability, with CXB-NPs showing an average particle size of 138.4 ± 4.3 nm and a zeta potential of –58.74 ± 16.58 mV. The system exhibited high porosity (87.16 ± 0.75%) and hydrophilicity (contact angle < 90°), achieved swelling equilibrium at 150 ± 10 min with a swelling ratio of 163.97 ± 9.76%, and degraded over 10 days with 88.53 ± 2.03% mass loss. Mechanical testing demonstrated high strength (Young's modulus 17.24 ± 2.65 MPa, elongation at break 307.48 ± 32.01%. NiN-HDS provided sustained CXB release over 7 days, reaching 67.16% cumulative release. In vivo, it reduced cartilage damage and suppressed IL-1β and MMP-13 expression, while maintaining mechanical support and controlled drug delivery.

Conclusion: In conclusion, we successfully developed NiN-HDS. Our results show that NiN-HDS combines sustained drug delivery with mechanical support, improves cartilage preservation and reduces local inflammation in a rat OA model, indicating that it can serve as a promising strategy for intra-articular therapy of osteoarthritis.

Keywords: osteoarthritis, nanoparticles, electrospinning, drug delivery, mechanical support

Introduction

Osteoarthritis (OA) is a common chronic degenerative joint disease affecting all joint tissues, in which persistent inflammation and abnormal joint biomechanics act as core pathological drivers, disrupting cartilage homeostasis and leading to progressive structural damage.[1,2] The knee joint, as the primary weight-bearing joint, is the most frequently

https://doi.org/10.2147/DDDT.S601447
Received: 16 February 2026
Accepted: 23 May 2026
Published: 8 June 2026

Graphical Abstract

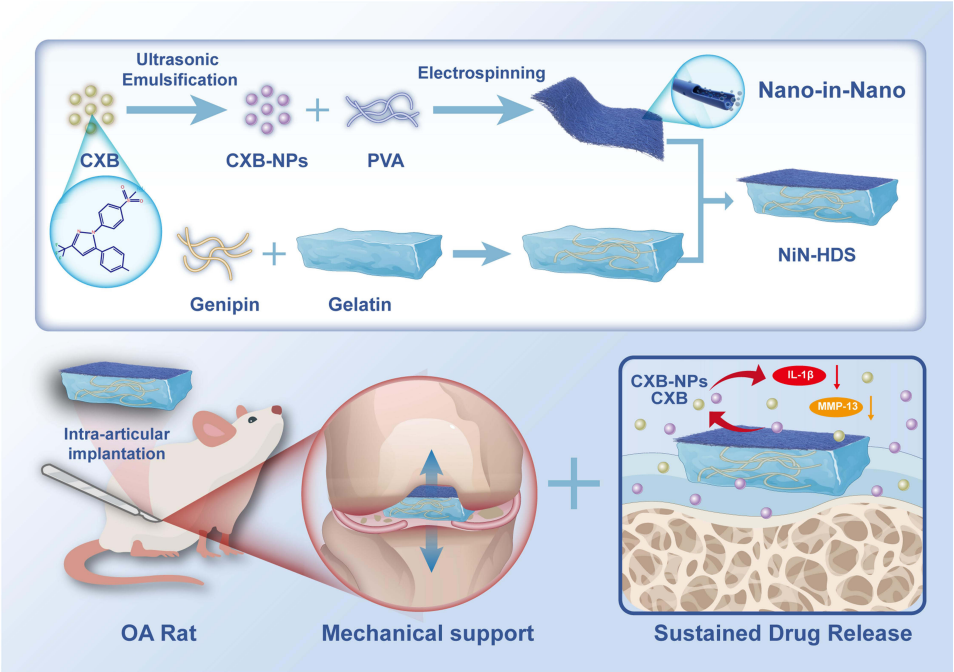

affected site of OA.[3] Under prolonged mechanical overload, mechanical signals activate mechanotransduction pathways such as Integrin-FAK, Wnt/β-catenin, and Hippo-YAP/TAZ, leading to the initiation of inflammatory signaling pathways, including NF-κB, JAK/STAT, and MAPK.[4] This cascade of signaling events triggers local inflammatory responses, releasing pro-inflammatory factors such as IL-1β, TNF-α, and matrix metalloproteinases (MMPs). These processes accelerate extracellular matrix degradation, disrupt cartilage structure, and promote chondrocyte apoptosis, sustaining a vicious cycle of "mechanical damage—inflammatory response—tissue degeneration".[5,6] Current pharmacological strategies for OA include non-steroidal anti-inflammatory drugs (NSAIDs, such as celecoxib), intra-articular corticosteroid injections, and hyaluronic acid supplementation.[7] While these treatments can effectively alleviate symptoms, they have notable limitations: oral or systemic administration may cause systemic adverse effects, such as gastrointestinal irritation, cardiovascular risk, and renal dysfunction;[8] the highly dense, avascular nature of articular cartilage makes it difficult for traditional delivery methods to reach the target site effectively;[9] moreover, rapid turnover of synovial fluid in the joint accelerates drug clearance, preventing oral or systemic administration from maintaining therapeutically effective concentrations locally, thereby significantly reducing treatment efficacy.[10]

Intra-articular drug delivery systems can partially overcome these limitations. Local administration not only prolongs drug retention and increases drug concentration within the joint, but also significantly reduces systemic adverse effects.[11] Hydrogels absorb water and swell, forming a stable intra-articular release environment and mimicking some lubricating properties of synovial fluid.[12] However, existing studies have rarely considered the responses and demands of articular cartilage within highly dynamic mechanical environments. In such a dynamic environment, repetitive compressive, shear, and sliding forces not only induce complex mechanical responses in cartilage but also affect the distribution and clearance of intra-articular drugs and their carriers through synovial fluid flow and interfacial friction, making it difficult for carriers to remain at the target site and accelerating drug loss.[13,14] Furthermore, as osteoarthritis progresses, the biomechanical properties of the joint undergo significant alterations, including decreased cartilage stiffness and abnormal load distribution.[15] These changes exacerbate cartilage matrix degradation and local inflammation and may further affect

the retention and diffusion of carriers within the joint, ultimately reducing therapeutic efficacy. Effective OA treatment thus requires not only sustained and stable anti-inflammatory drug delivery but also appropriate modulation of the local joint mechanical environment and provision of mechanical support. However, when drug delivery and mechanical support are integrated within a single system, achieving optimal performance for both is challenging, as increasing mechanical stiffness is often accompanied by a reduction in drug diffusion efficiency. The development of an intra-articular implant system that provides sustained drug delivery and adaptive mechanical support, therefore, is still a significant challenge, as it must address the dual problems of rapid drug clearance and mechanical imbalance.

Poly(lactic-co-glycolic acid) (PLGA) is a biodegradable and biocompatible copolymer whose drug-release kinetics can be regulated by modifying its monomer ratio and molecular weight,[16] providing a stable platform for the sustained local delivery of poorly soluble drugs such as celecoxib. Electrospinning applies a high-voltage electric field to process drug-loaded nanoparticles into continuous nanofibers, resulting in a "Nano-in-Nano" architecture.[17] This configuration enhances drug stability, prolongs release, and increases loading capacity. Drug-loaded nanoparticles were embedded within a PVA nanofiber membrane via electrospinning. Although PVA is inherently highly water-soluble and prone to rapid dissolution in synovial fluid, the electrospun fibers form a stable three-dimensional network that allows the drug-loaded membrane to persist in the aqueous joint environment for extended periods, providing a platform for sustained drug release.[18] The electrospun nanofibers also exhibit a high surface area and a porous, extracellular matrix (ECM)-like morphology, which aids efficient drug loading and localized delivery.[19] Gelatin, a polypeptide derived from collagen hydrolysis, offers excellent biocompatibility and degradability, and its mechanical properties can be tuned via cross-linking to adjust to the dynamic loads of joint movement.[20] In this study, a hierarchical "nanoparticle-nanofiber-gelatin layer" structure was used to separate drug delivery from mechanical support: the electrospun nanofiber membrane serves as a sustained-release drug delivery layer, while the gelatin layer provides tunable mechanical support, offering flexible reinforcement for the implant. This design enables the synergistic optimization of both functions. Celecoxib (CXB) was loaded into PLGA nanoparticles (CXB-NPs) using an emulsion solvent evaporation method. These CXB-NPs were incorporated into a "Nano-in-Nano" nanofiber membrane via electrospinning, and the drug-loaded nanofiber membrane was combined with gelatin layers to form the Celecoxib-Loaded "Nano-in-Nano" Hierarchical Delivery System (NiN-HDS). NiN-HDS was systematically evaluated for its physicochemical properties, drug-loading capacity, in vitro release profile, implantation stability, and therapeutic potency in a rat OA model. The objective was to develop a novel intra-articular implant strategy that integrates sustained drug delivery with mechanical regulation aimed at comprehensive OA management.

Materials and Methods

Materials

Polyvinyl alcohol (PVA 04–88 and PVA 17–99) was obtained from Kuraray Trading Co., Ltd. (Shanghai, China). 2-Hydroxypropyl-β-cyclodextrin (2-HP-β-CD) was supplied by Zibo Qianhui Biotechnology Co., Ltd. (Zibo, China). Celecoxib was purchased from Aladdin Biochemical Technology Co., Ltd. (Shanghai, China). Poly(lactic-co-glycolic acid) (PLGA) was sourced from Jinan Joyful Biological Technology Co., Ltd. (Jinan, China). Gelatin was also acquired from Aladdin Biochemical Technology Co., Ltd. (Shanghai, China). Monosodium iodoacetate (MIA) was supplied by Sigma-Aldrich (St. Louis, MO, USA). Celecoxib capsules were provided by Pfizer Inc. (New York, NY, USA). All other reagents and organic solvents were of analytical grade.

Preparation of NiN-HDS

CXB-NPs were first fabricated using an emulsion solvent evaporation method,[21] following a previously established protocol. These CXB-NPs were then incorporated into electrospun nanofibers using PVA 17–99 as the film-forming matrix, forming a "Nano-in-Nano" structured nanofiber membrane. Finally, the nanofiber membrane was laminated with a genipin-crosslinked gelatin layer to form the NiN-HDS. Specifically, celecoxib (10 mg) and PLGA (50 mg) were dissolved in an acetone-dichloromethane mixture (3:2, v/v) to form the oil phase. The aqueous phase consisted of a 2% 2-HP-β-CD and 1.5% PVA 04–88 aqueous solution. Under ice bath conditions (0–4°C), the oil phase was slowly injected

into the aqueous phase and emulsified ultrasonically (amplitude probe φ6 mm, 150 kHz; JY92-IIDN, Shanghai Huxi Industrial Co., Ltd). After 90 seconds of emulsification, the organic solvent was removed by rotary evaporation (RE801, Yamato Co., Japan) with heating, and the volume was adjusted with distilled water. A 10% PVA 17–99 (w/v) solution was added as a film-forming agent to the nanoparticle suspension, which was then stirred at 85°C for 2 hours to prepare the spinning solution. Electrospinning was performed at 18 kV with a feed rate of 0.7 mL·h-1 and a 140 mm collecting distance using a single-needle setup (27G, outer diameter 0.41 mm, inner diameter 0.20 mm; NAN0N-01A, MECC, Japan). The resulting nanofiber membrane was dried for 12 hours to obtain the drug-loaded membrane. Separately, gelatin and distilled water (1:1, w/w) were mixed and stirred at 80°C until fully dissolved. Glycerol was added at a mass ratio of gelatin: glycerol: water = 1:0.5:1, and the mixture was stirred for 30 minutes and held at 80°C for 1 hour to degas. This solution was cast into a mold to form a 0.5 mm thick layer and cured at 30°C for 1 hour. The gelatin layer was then immersed in a 1% genipin-ethanol solution (w/v) and crosslinked in the dark at 37°C for 30 minutes. After crosslinking, the layer was rinsed three times with PBS (pH 7.4). Finally, a thin coating of gelatin solution was applied to the nanofiber membrane, which was attached to the gelatin layer to complete the NiN-HDS.

A Blank Hierarchical Delivery System (Blank-HDS) and a Directly Celecoxib-loaded Nanofibrous Hierarchical Delivery System (CXB-NF-HDS) were also prepared to assess how drug loading and its method influence fiber morphology and drug release. Their preparation differed from that of the NiN-HDS only in the presence of the drug and whether it was loaded into the PLGA matrix. All other procedural steps were identical.

Nanocarrier Size, Polydispersity, and Particle Charge

The particle size distribution, polydispersity index (PDI), and zeta potential of the CXB-NPs loaded within the NiN-HDS were characterized using a Delsa Nano C Nanoparticle Size/Zeta Potential Analyzer (Beckman Coulter, Inc., Brea, CA, USA). For analysis, a small quantity of NiN-HDS was weighed, dissolved in pure water, and the scattering intensity was adjusted to 10,500 ± 1,500 cps before measurement.

Shape and Morphology

Microscopic Characteristics of CXB-NPs and NiN-HDS

For CXB-NPs, morphology was observed by transmission electron microscopy (TEM; JEOL JEM-1400, JEOL Ltd., Tokyo, Japan) using negative staining.[22] A copper grid was immersed in the CXB-NPs solution for 10 minutes, stained with 2% tungstic acid for a further 10 minutes, and blotted with filter paper to remove excess solution. After air-drying, the grid was imaged. For NiN-HDS, samples were collected directly by placing a copper grid on the electrospinning collector during the spinning process. TEM imaging directly revealed the morphology, size, and distribution of nanoparticles within the nanofibers, providing key structural knowledge of the NiN-HDS system.

Morphology and Diameter Distribution of Nanofibers

A scanning electron microscope (SEM; Gemini SEM300, ZEISS, Oberkochen, Germany) was used to examine the surface morphology of the electrospun nanofibers and determine their diameter distribution. The samples were sectioned to a suitable size, sputter-coated with gold for 90 seconds, and affixed to a sample holder with conductive adhesive for imaging at 15 kV. The resulting micrographs of NiN-HDS were analyzed using ImageJ software (1.52P, Wayne Rasband, National Institutes of Health, Bethesda, MD, US). The diameters of 100 individual fibers were measured to generate a histogram, thereby evaluating the uniformity and size distribution of the fiber population.

Encapsulation Efficiency and Drug Loading Capacity

The encapsulation efficiency (EE%) and drug loading (DL%) of celecoxib in CXB-NPs were quantified by high-performance liquid chromatography (HPLC, e2695, Waters Corporation, Milford, MA, USA) using an ultrafiltration-centrifugation method[23,24] Briefly, a sample of the CXB-NPs solution was centrifuged at 1,000 rpm for 10 minutes to sediment any large aggregates. The resulting supernatant, containing the nanoparticles and a minor fraction of dissolved free drug, was transferred to a 3 kDa molecular weight cutoff ultrafiltration tube. This tube was then centrifuged at 15,000 rpm (TDL-60B, Shanghai) at 4°C for 30 minutes. The PLGA nanoparticles, being substantially larger than 3 kDa,

were retained in the ultrafiltration device, while the free drug passed into the filtrate. This achieved a complete separation of the encapsulated drug from its free counterpart. Encapsulation efficiency and drug loading were subsequently calculated using equations (1) and (2). HPLC determined the celecoxib content under the following conditions: a Hypersil ODS C18 column (250 mm × 4.6 mm, 5 μm), a mobile phase of methanol-water (85:15), an injection volume of 10 μL, a flow rate of 1 mL/min, a column temperature of 25°C, and a detection wavelength of 254 nm.

$$EE\% = \frac{C_1 - C_2}{C_0} \times 100\% \quad (1)$$

$$DL\% = \frac{(C_1 - C_2)V}{M} \times 100\% \quad (2)$$

In these formulas, C_0 denotes the initial drug concentration ($\mu g \cdot mL^{-1}$), while C_1 is the drug concentration in the supernatant following low-speed centrifugation ($\mu g \cdot mL^{-1}$). The term C_2 represents the drug concentration in the filtrate from the ultrafiltration tube ($\mu g \cdot mL^{-1}$). Here, V corresponds to the volume of the drug-loaded nanoparticles (mL), and M signifies the total mass of celecoxib and PLGA within the drug-loaded nanoparticles (mg).

Drug–Carrier Interaction of NiN-HDS

To determine the crystalline form of CXB within the NiN-HDS, we analyzed the raw drug, CXB-NF-HDS, and NiN-HDS using differential scanning calorimetry (DSC, DSC4000, PerkinElmer, Waltham, MA, USA), Fourier transform infrared spectroscopy (FTIR, Nicolet iS5, Thermo Fisher Scientific, Waltham, MA, USA), and X-ray diffraction (XRD, Rigaku SmartLab SE, Rigaku Corporation, Tokyo, Japan). These analyses assessed the solid-state of CXB and probed its molecular bonds with the carrier material.

Differential Scanning Calorimetry (DSC)

DSC assessed the physical and chemical changes associated with the crystalline form and thermal behavior of the samples.[25] Approximately 5 mg of this CXB raw drug, CXB-NF-HDS, and NiN-HDS samples were each sealed in an aluminum crucible. The temperature was increased from 30°C to 300°C at a heating rate of $10°C \cdot min^{-1}$. The thermal analysis was performed under a nitrogen flow of $20\ mL \cdot min^{-1}$.

X-Ray Diffraction (XRD)

XRD was subsequently used to identify the crystalline form of CXB within the CXB-NF-HDS and NiN-HDS systems.[26] The measurements were carried out using a Cu rotating anode X-ray source operating at 9 kW, with a tube voltage of 45 kV and a current of 200 mA. Data were collected over a 2θ range from 5° to 90° at a scanning speed of of $0.02° \cdot s^{-1}$.

Fourier Transform Infrared Spectroscopy (FTIR)

FTIR was used to characterize the interaction between CXB and the carrier.[27] Samples of CXB, CXB-NF-HDS, and NiN-HDS were dried, and 2 mg of each was mixed and ground with 100 mg of potassium bromide (KBr). The resulting mixture was pressed into a KBr pellet. This pellet was then scanned at room temperature across the spectral range of 4000 to 400 cm^{-1}.

The Swelling, Degradation, and Drug Release Profile Study

Since excessive swelling can compromise the physical structure and mechanical properties of NiN-HDS, this parameter constitutes an essential indicator of intra-articular implant adaptability.[28] The initial sample weight (W_1) was recorded to evaluate swelling behavior. Each sample was immersed in pure water at 37°C, removed at 15-minute intervals, blotted with filter paper to remove surface moisture, and weighed (W_2) until swelling equilibrium was achieved. The swelling ratios of Blank-HDS, CXB-NF-HDS, and NiN-HDS were determined experimentally and calculated using formula (3).

$$\text{Swelling ratio} = \frac{W_2 - W_1}{W_1} \times 100\% \quad (3)$$

 https://doi.org/10.2147/DDDT.S601447

To assess in vitro degradation, the weight loss method was employed. After freeze-drying and weighing (W_1), samples were placed in PBS buffer (pH 7.4) at 37°C. Every 24 hours, they were removed, rinsed three times with ultrapure water, freeze-dried again, and reweighed (W_2). This degradation process was monitored over 14 days, with the degradation rate for each formulation calculated using formula (4).

$$\text{Degradation ratio} = \frac{W_1 - W_2}{W_1} \times 100\% \tag{4}$$

To simulate the distinct microenvironments of normal and osteoarthritic joint cavities, phosphate-buffered saline (PBS) at pH 6.8 and pH 7.4, each containing 0.5% SDS, served as the in vitro release media. The dialysis bag method compared the release profiles of celecoxib from CXB-NPs, CXB-NF-HDS, and NiN-HDS to evaluate the effects of different drug-loading strategies.[29] Specifically, 1 mL of CXB solution, 1 mL of CXB-NPs solution, and 25 mg of CXB-NF-HDS and NiN-HDS were sealed in dialysis bags (6 cm, MWCO 8,000–14,000) and immersed in 30 mL of release medium within 50 mL centrifuge tubes. The tubes were incubated in a constant-temperature shaker (IS-RSV3, JieMei, Suzhou, China) at 37°C and 120 rpm. At predetermined intervals (1, 2, 4, 8, 12, 24, 48, 72, 96, 120, 144, and 168 hours), 2 mL of medium was sampled and replaced with an equal volume of fresh medium. The collected samples were filtered (0.22 μm) and analyzed for CXB content via HPLC under the following conditions: Kromasil 100-5-C18 column (4.6 mm × 250 mm); mobile phase of methanol-water (85:15, v/v); column temperature of 25°C; flow rate of 1.0 $mL \cdot min^{-1}$; injection volume of 20 μL; and detection wavelength of 254 nm. The in vitro release curves were plotted, and the cumulative release was calculated using formula (5).

$$Q = \frac{V_1 C_t + V_2 \sum_{t-1} C_{t-1}}{m_0} \times 100\% \tag{5}$$

In this formula, Q is the cumulative drug release percentage (%); V_1 is the total volume of release medium (30 mL); V_2 is the sample volume (2 mL); C_t is the drug concentration at time t ($\mu g \cdot mL^{-1}$); and m_0 is the initial drug load (mg).

Performance Test of NiN-HDS

Electrospun nanofibers have small diameters and large surface areas, which support cell adhesion and drug release. However, their mechanical properties are limited. Adding gelatin can effectively improve these properties. Consequently, the NiN-HDS design combines mechanical support with the multifunctional benefits of a "Nano-in-Nano" architecture. To assess its suitability for intra-articular implantation, we comprehensively evaluated the sample's cell adhesion interface properties, wettability, and mechanical compatibility by measuring porosity, contact angle, and mechanical performance.

Sample porosity was determined via Archimedes principle using a pycnometer with anhydrous ethanol as the displacement medium.[30] First, Blank-HDS, CXB-NF-HDS, and NiN-HDS samples of similar volume were selected, and their dry mass (M_1) was recorded. Each sample was then placed into a pycnometer filled with anhydrous ethanol, and the combined mass (M_2) was measured. After mixing, the total mass (M_3) of the sample and ethanol was recorded. The samples were fully immersed and subjected to repeated vacuum-vent cycles to ensure complete ethanol infiltration into the scaffold pores without apparent bubbles; they were then removed. The mass of the remaining ethanol and pycnometer was then recorded as M_4. The porosity of each sample type was calculated using formula (6).

$$\text{Porosity}(\%) = \frac{M_3 - M_4 - M_1}{M_2 - M_4} \times 100\% \tag{6}$$

The contact angle indicates surface wettability; a smaller angle indicates greater wettability.[31]

We analyzed the wettability of the NiN-HDS surface using a contact angle goniometer (SDC-100, DingSheng, Dongguan, China). Different samples were cut to size and placed horizontally on the instrument stage. A micro-syringe with a flat needle was used to deposit a droplet of deionized water onto the sample surface. The droplet shape upon contact was captured, and the instantaneous contact angle was measured using ImageJ software.

Suitable mechanical properties are a key prerequisite for intra-articular implantation.[32] We evaluated these properties through Young's modulus, fracture strength, and elongation at break. Stress-strain curves were obtained using a texture

analyzer (TA-XTplus, Stable Micro Systems, Godalming, UK). Samples were cut to dimensions of 50×10 mm and tested with an A/TG probe using a 30 mm grip distance and a 10 mm grip length. The tests were conducted at a stretching speed of 200 mm·min^{-1}. Young's modulus, fracture strength, and elongation were derived from the stress-strain curves to assess the deformation process, capacity, and extent for Blank-HDS, CXB-NF-HDS, and NiN-HDS.

In vivo Safety and Efficacy Evaluation

The intra-articular injection of sodium iodoacetate into the knee joint produces a classical and reliable model of OA.[33] This model recapitulates key clinical features of the disease, including joint pain, intermittent inflammation, and neural damage. Given that a 20 μg dose of celecoxib delivered directly to cartilage significantly inhibits inflammatory damage,[34] we investigated the pathological effects of the system on rat knee cartilage to quantitatively evaluate the impact of NiN-HDS on OA. This intra-articular administration ensures sufficient local drug concentration despite the relatively low absolute dose. All procedures were approved by the Institutional Animal Care and Use Committee of Guangdong Pharmaceutical University and complied with the National Institutes of Health Guide for the Care and Use of Laboratory Animals. Following a 3-day acclimatization period, all rats except those in the normal group (n=8) were anesthetized via intraperitoneal injection of 2% pentobarbital sodium (40 mg·kg−^{1}). With the knee flexed at 45°, a 50 μL volume of 2% MIA solution (2 μg/100 μL in 0.9% saline) was injected laterally through the patellar ligament into the joint cavity. The knee was then flexed and extended repeatedly for 30 seconds to distribute the solution. All animals were subsequently housed in standard conditions. Hind limb strength (XR-YLS-13A; Xinsoft Information Technology Co., Ltd, Shanghai, China) and behavioral changes were assessed every 7 days using the Lequesne MG score.[35] At day 28, the rats were randomly allocated into four groups (n=8 per group): a model group, a CXB group, a sham surgery group, and a NiN-HDS group. The CXB group received 10.5 mg·kg^{-1} celecoxib capsules by oral gavage once daily. For the NiN-HDS treatment group, the injection site was disinfected and anesthetized, and the joint cavity was opened. Sterilized NiN-HDS (thickness 0.5 mm, lateral dimensions ~3.2 mm × 3.2 mm; containing approximately 20 μg of celecoxib) were implanted, with the nanofiber membrane surface placed in contact with the femoral trochlear cartilage. The joint cavity and skin were then sutured closed in layers. The NiN-HDS was sterilized using ultraviolet (UV) irradiation for 30 minutes prior to implantation. The sham surgery group underwent an identical procedure without drug implantation. To prevent postoperative infection, all surgical rats received an intramuscular injection of 30,000 units of penicillin daily for 3 days. The materials used in NiN-HDS have all been demonstrated to be biocompatible in published studies and have been widely employed in FDA-approved biomedical applications. All procedures were performed under sterile conditions, and no signs of infection, systemic inflammation, or abnormal behavior were observed in any animals during the study period. Seven days after treatment initiation, rats were euthanized with an overdose of 2% pentobarbital sodium. The skin and subcutaneous tissue overlying the bilateral knee joints were dissected, and surrounding muscle was removed to isolate the entire knee joint, retaining the distal quarter of the femur and proximal quarter of the tibia. The joints were photographed for gross evaluation of cartilage damage using the Pelletier scoring system.[36] After fixation in 4% paraformaldehyde and decalcification in 5% EDTA, samples were paraffin-embedded, sectioned, and stained with H&E and Safranin O-fast green. Histopathological changes were assessed microscopically and scored using the Mankin system.[37] Immunohistochemistry was performed to assess the expression of IL-1β and MMP-13. Primary antibodies were applied as follows: anti-IL-1β (Proteintech, 1:300) and anti-MMP-13 (Proteintech, 1:300). Secondary antibodies conjugated with horseradish peroxidase were used according to the manufacturer's instructions. Positive cells were semi-quantitatively evaluated using ImageJ software.

Statistical Analysis

Statistical analyses were performed using GraphPad Prism 8.0.2 (GraphPad Software, San Diego, CA, USA; www.graphpad.com), with data expressed as the mean ± standard deviation. For comparisons between two specific groups, a two-tailed Student's *t*-test was applied. For comparisons of multiple experimental groups versus the model group, a one-way ANOVA followed by Dunnett's multiple-comparison test was used. Pairwise comparisons among all groups were performed using Tukey's honestly significant difference (HSD) test. Data were verified to meet the assumptions of the tests (normality and homogeneity of variance). A p-value < 0.05 was considered statistically significant.

Results and Discussion

Rational Design and Structural Characterization of the "Nano-in-Nano" NiN-HDS

Compared with traditional systems such as microspheres, nanoparticles more readily cross biological barriers in inflamed tissues, thereby enhancing drug penetration at the inflammatory site.[38] As shown in Figure 1A, the prepared CXB-NPs dispersion is clear and transparent and exhibits a faint bluish sheen, which is characteristic of a typical nanoscale particle size. TEM imaging showed spherical particles (Figure 1B) with an average size of (64.90 ± 0.57) nm, a PDI of 0.142 ± 0.004 (Figure 1D), and a zeta potential of −(13.29 ± 0.35) mV (Figure 1E), showing a uniform size distribution, good dispersibility, and system steadiness. Within the NiN-HDS system, CXB-NPs retained their nanostructure after electrospinning and re-dissolution, as observed by TEM (Figure 1C). Their average particle size increased to (138.4 ± 4.3) nm, with a PDI of 0.180 ± 0.082 (Figure 1F) and a zeta potential of –(58.74 ± 16.58) mV (Figure 1G). Compared to free CXB-NPs, the spun CXB-NPs exhibited an approximately two-fold increase in particle size and a significantly higher absolute zeta potential. Such enhanced zeta potential indicates stronger electrostatic repulsion, therefore stabilizing the

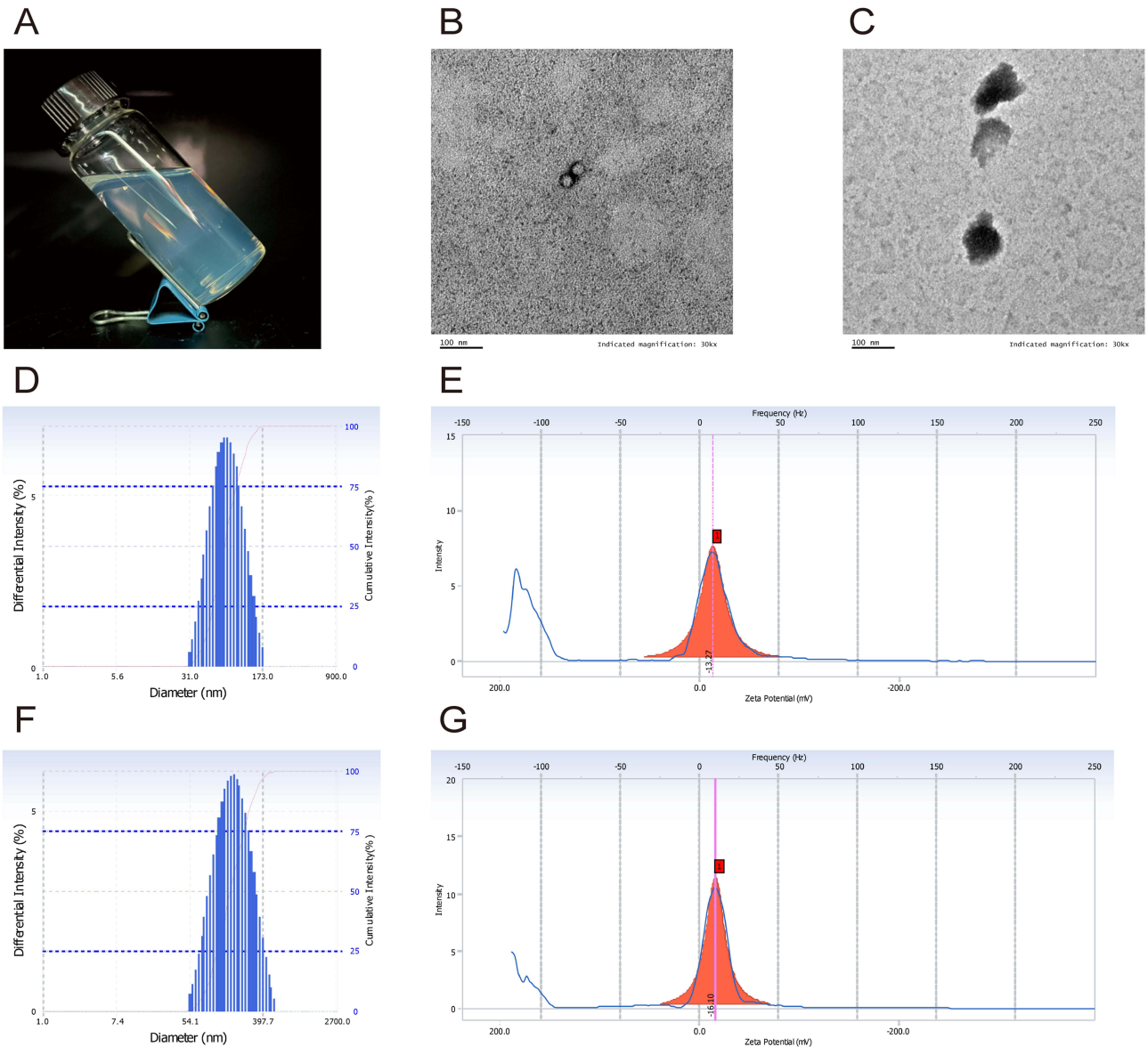

Figure 1 Characterization of CXB-NPs. (**A**) Appearance properties. (**B**) TEM image of CXB-NPs. (**C**) TEM image of CXB-NPs recovered from the nanofibrous membrane. (**D**) Particle size distribution of CXB-NPs. (**E**) Zeta potential of CXB-NPs. (**F**) Particle size distribution of CXB-NPs recovered from the nanofibrous membrane. (**G**) Zeta potential of CXB-NPs recovered from the nanofibrous membrane. Results are based on three independent experiments.

https://doi.org/10.2147/DDDT.S601447

nanoparticles and preventing their aggregation.[39] Furthermore, the particle sizes measured by TEM agreed with those from the particle size analyzer, confirming that CXB-NPs maintain good structural stability after high-temperature treatment and electrospinning, with minimal alteration to their nanostructure during membrane formation. To determine drug content across formulations, we established and validated a high-performance liquid chromatography (HPLC) method. The measured CXB content was (513.81 ± 1.41) $\mu g \cdot mL^{-1}$ in CXB-NPs, (3.94 ± 0.14) $\mu g \cdot mL^{-1}$ in CXB-NF-HDS, and (3.54 ± 0.09) $\mu g \cdot mL^{-1}$ in NiN-HDS. Using the ultrafiltration-centrifugation method, the encapsulation efficiency of CXB-NPs was (72.87 ± 0.30)% with a drug loading of (1.50 ± 0.01)%.

The structural design of this system decouples drug delivery from mechanical support by assigning these functions to a drug-loaded nanofiber membrane and a gelatin layer, respectively, enabling their combined optimization. Under optical microscopy (Figure 2A), the nanofiber membrane displayed a continuous, disordered fibrous structure with good fiber formation, with no apparent bead defects or fiber aggregation; the presence of the drug did not substantially change the fiber morphology. TEM imaging (Figure 2B) revealed uniform fibers with smooth surfaces, suggesting that adsorption of

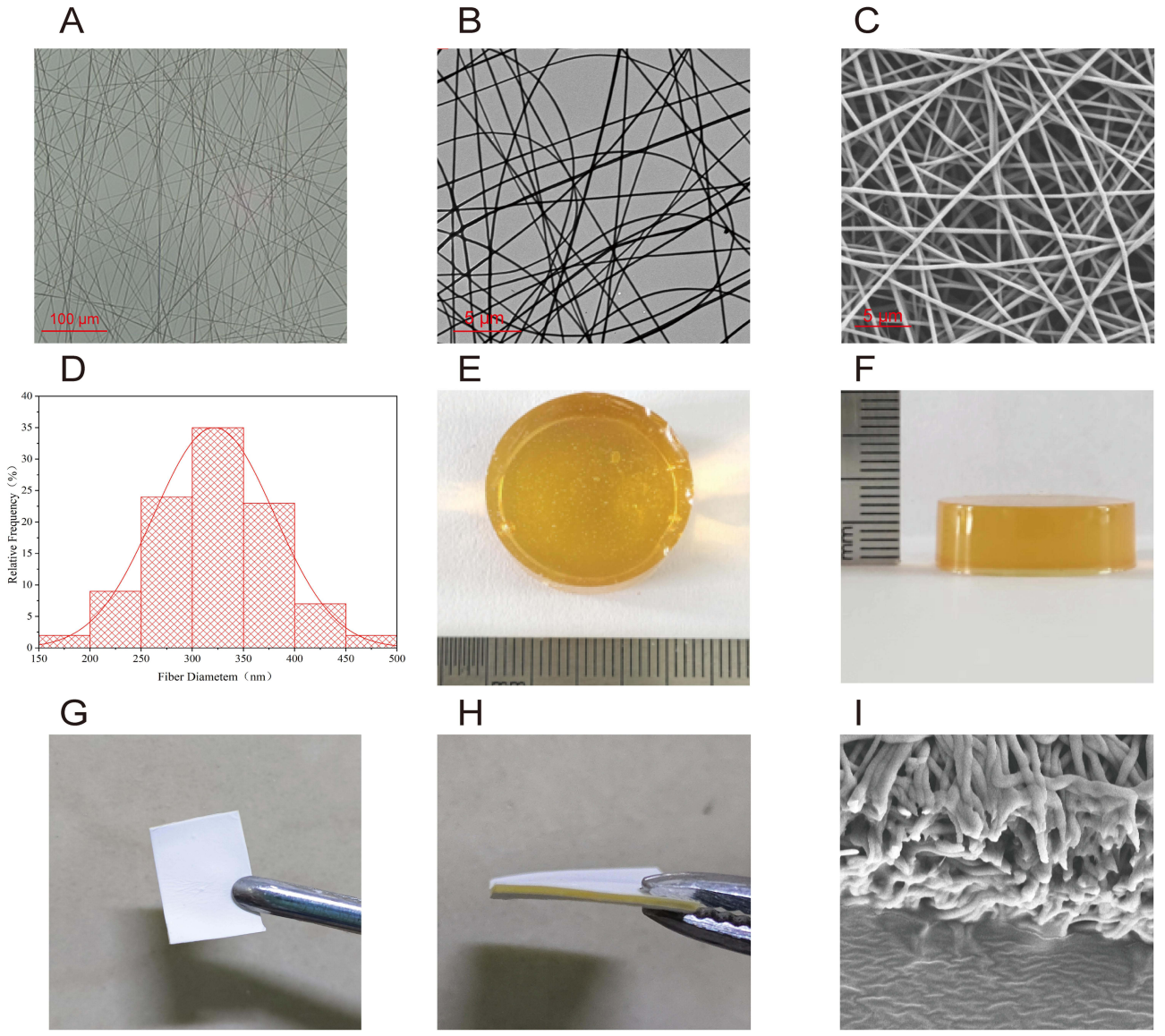

Figure 2 Morphological characterization of the nanofibrous membrane, gelatin layer, and NiN-HDS. (**A**) Optical microscopy image of the nanofibrous membrane. (**B**) TEM image of the nanofibrous membrane. (**C**) SEM image of the nanofibrous membrane. (**D**) Diameter distribution of nanofibers measured from SEM images (n = 100 fibers). (**E**) Macroscopic appearance of the gelatin layer. (**F**) Side view of the gelatin layer. (**G**) Macroscopic appearance of NiN-HDS. (**H**) Side view of NiN-HDS. (**I**) SEM image showing the interfacial contact between the nanofibrous membrane and gelatin layer within NiN-HDS. Results are based on three independent experiments.

https://doi.org/10.2147/DDDT.S601447

the hydrophilic polymer PVA onto the CXB-NP surfaces inhibited local nanoparticle aggregation within the fibers and prevented accumulation on the fiber surfaces.[18] Statistical analysis of 100 fibers from the same field of view by SEM (Figure 2C and D) indicated an average NiN-HDS fiber diameter of 145.95 ± 26.05 nm, with a relatively uniform distribution. The gelatin layer appeared smooth, uniform, and highly transparent (Figure 2E), while a side view (Figure 2F) confirmed an even thickness. The composite NiN-HDS was white and opaque, with a thickness of approximately 0.5 mm (Figures 2G and H). SEM examination (Figure 2I) revealed tight bonding at the interface between the nanofiber and gelatin layers, with no visible gaps, confirming the successful assembly of the composite structure without disrupting the inherent characteristics of either layer.

CXB, a BCS Class II drug, exhibits poor water solubility, limiting dissolution and absorption in oral formulations and therewith compromising its bioavailability and efficacy. Formulating celecoxib within an amorphous nanocarrier can suppress crystallization and significantly improve its dissolution rate and bioavailability.[40] The physical state of CXB within the formulation was investigated using FTIR, DSC, and XRD. FTIR spectra of raw CXB (Figure 3A) showed characteristic sulfonyl group (S=O and S-O) stretching vibrations at 1,133 cm^{-1} and 1,345 cm^{-1}, along with C-H and N-H peaks at 3,232 cm^{-1} and 3,339 cm^{-1}.[41] In the CXB-NF-HDS formulation, these sulfonyl peaks were attenuated, and a broad band emerged between 3050 and 3,450 cm^{-1}, attributable to overlapping O-H, C-H, and N-H vibrations, indicating hydrogen bonding between the drug and carrier. These characteristic peaks were substantially weakened or absent in NiN-HDS, denoting a transition of CXB from a crystalline to an amorphous state. DSC thermograms revealed a sharp endothermic peak near 169.49°C for raw CXB, corresponding to its crystalline melting point (Figure 3B).[42] This peak was virtually absent in CXB-NF-HDS, implying that CXB underwent a phase change during electrospinning to an amorphous or semi-crystalline form. Similarly, no endothermic peak was detected for NiN-HDS, further confirming the amorphization of CXB during nanoparticle encapsulation and electrospinning and indicating that its interaction with the PLGA carrier involved more than simple physical adsorption, resulting in an amorphous composite. XRD patterns provided additional support: raw CXB exhibited numerous sharp, intense diffraction peaks across the 5°–40° range, attesting to its crystalline nature (Figure 3C).[43] These characteristic peaks disappeared in both CXB-NF-HDS and NiN-HDS, displaying a marked reduction in crystallinity and an amorphous dispersion of the drug. Collectively, these data indicate that during electrospinning, CXB engages in intermolecular interactions with the polymer matrix, stabilizing in an amorphous form. The random molecular arrangement and higher free energy of the amorphous state eliminate the need to overcome lattice energy during dissolution, consequently enhancing the formulation's solubility, release profile, and stability.

Structure-Mediated Dual Functional Performance

Good wettability enhances adhesion between the implanted system and cartilage tissue. The instantaneous contact angles for Blank-HDS, CXB-NF-HDS, and NiN-HDS were all below 90° (Figure 4A), confirming their hydrophilic surfaces. This hydrophilicity stems primarily from the native hydroxyl groups (-OH) on PVA molecules.[44] Following the loading

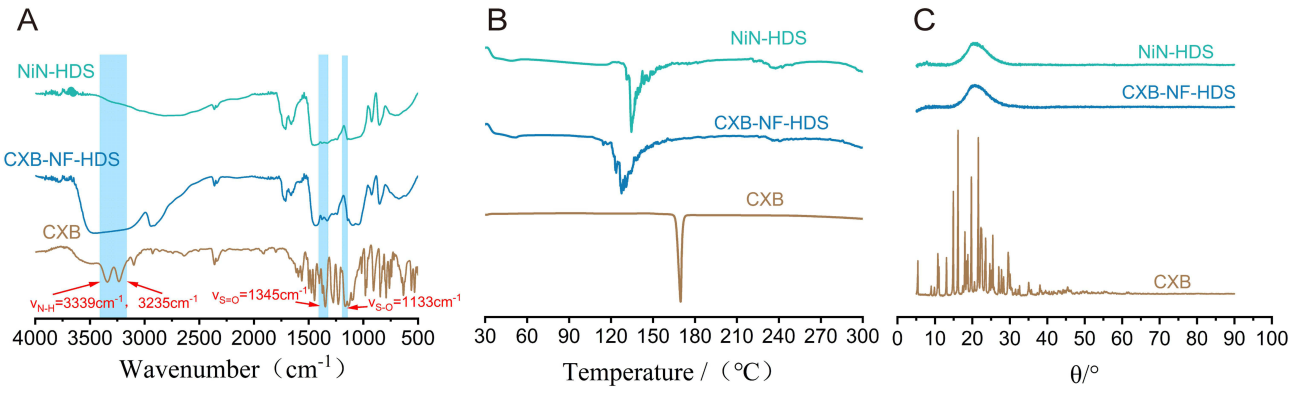

Figure 3 Analysis of drug–carrier interactions by FTIR, DSC, and XRD. (**A**) FTIR spectra. (**B**) DSC thermograms. (**C**) XRD patterns of CXB, CXB-NF-HDS, and NiN-HDS.

 https://doi.org/10.2147/DDDT.S601447

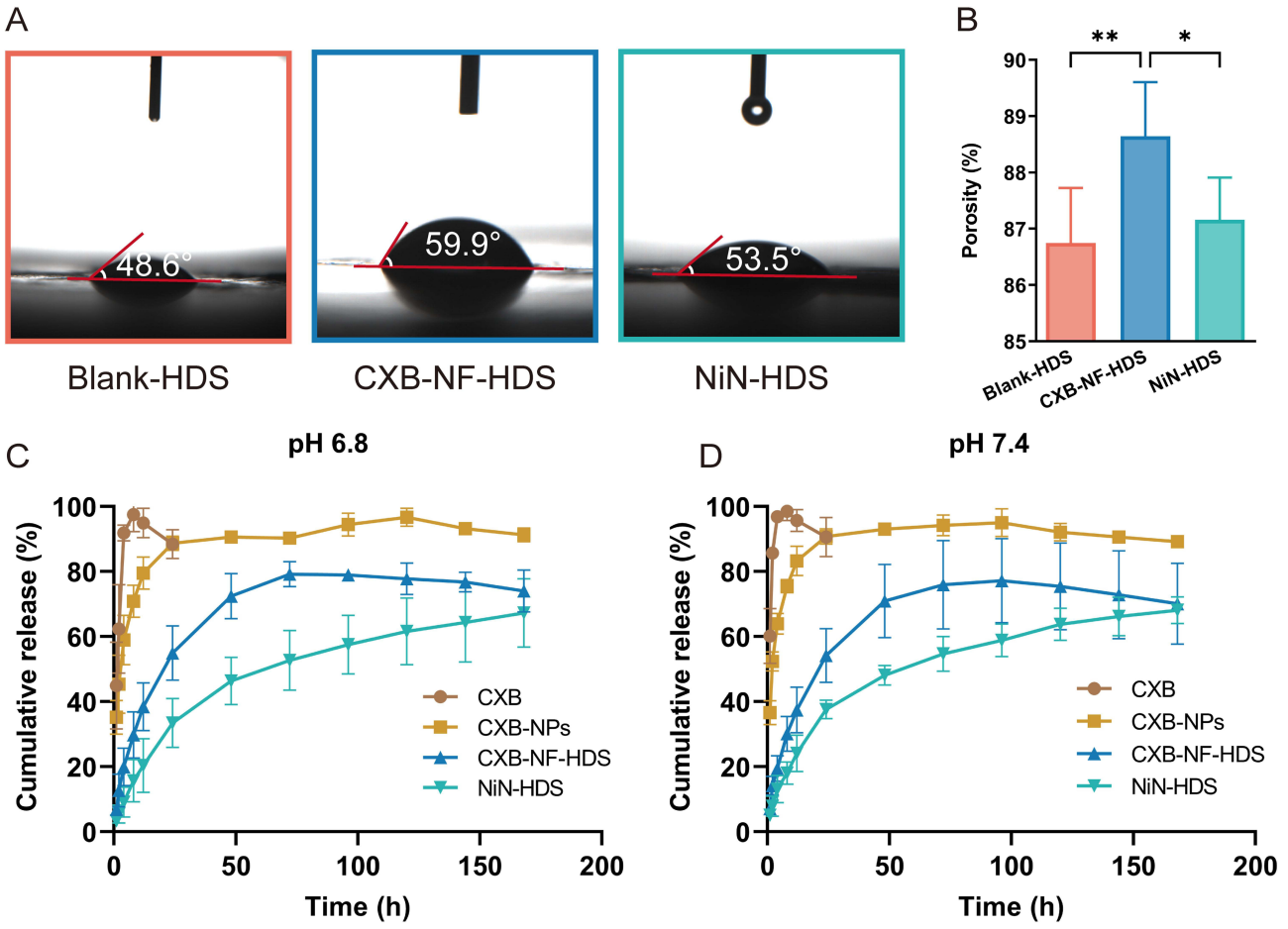

Figure 4 Instantaneous water contact angle, porosity, and in vitro drug release behaviors of different formulations. (**A**) Instantaneous water contact angles of Blank-HDS, CXB-NF-HDS, and NiN-HDS. (**B**) Porosity of Blank-HDS, CXB-NF-HDS, and NiN-HDS. (**C**) In vitro cumulative release profiles of CXB, CXB-NPs, CXB-NF-HDS, and NiN-HDS at pH 6.8. (**D**) In vitro cumulative release profiles of CXB, CXB-NPs, CXB-NF-HDS, and NiN-HDS at pH 7.4. Each value represents the mean ± SD of three experiments for (A) and six experiments for (**B**–**D**). (*$P < 0.05$; **$P < 0.01$).

of hydrophobic CXB, the wettability of NiN-HDS remained essentially unchanged, indicating the drug-loaded nanoparticles were effectively encapsulated within the fibers without altering the surface chemistry. The porosity test results (Figure 4B) show that the porosities of Blank-HDS, CXB-NF-HDS, and NiN-HDS all ranged between 86.7% and 88.7%, with NiN-HDS exhibiting a porosity of 87.16 ± 0.75%.

The in vitro release profiles (Figure 4C and D) show clear release behaviors among the formulations. Raw CXB rapidly achieved a saturated concentration, whereas CXB-NPs released 45.40% and 52.36% of the drug within the first 2 hours in pH 6.8 and pH 7.4 media, respectively. This initial burst release likely results from structural relaxation and the rapid diffusion of surface-adsorbed drug molecules.[45] Subsequently, influenced by the slow swelling of PLGA, the drug was released gradually until reaching peak release at 120 hours (pH 6.8) and 96 hours (pH 7.4), with cumulative release rates of 96.70% and 95.08%, respectively. These results present a pronounced sustained-release effect compared with the raw drug, confirming that the PLGA nanocarrier effectively retards drug release. CXB-NF-HDS, prepared by directly electrospinning raw CXB, attained maximum release at 96 hours, with cumulative releases of 78.92% and 77.22% at pH 6.8 and pH 7.4. This indicates that the fiber pore structure serves as a physical diffusion barrier, partially delaying release. In contrast, NiN-HDS showed cumulative releases of 67.16% and 68.22% at 168 hours, exhibiting a further slowed release rate. This is mainly due to its unique "Nano-in-Nano" structure, which combines the controlled-release properties of nanoparticles with the physical barrier effect of the fiber matrix. The multilayered architecture synergistically modulates drug release kinetics, yielding superior long-term release performance. NiN-HDS thus exhibits favorable sustained-release properties across various pH conditions, making it well-suited to the complex pathological environment

https://doi.org/10.2147/DDDT.S601447

of OA joints, which entails rapid synovial fluid turnover, drug clearance, and mild acidic inflammation. Kinetic models were fitted to the release data for each formulation. The fitting results (Table 1) indicate that pH 6.8 and pH 7.4 did not alter the applicable release model, demonstrating that drug release from the formulations proceeded normally under both osteoarthritic and normal physiological conditions. Both CXB-NPs and CXB-NF-HDS followed first-order kinetics, consistent with a constant elimination rate. In contrast, the release from NiN-HDS was best described by the Ritger-Peppas equation. At pH 6.8, the release exponent n was 0.45269, a value between 0.45 and 0.89, showing a release mechanism combining Fickian diffusion and matrix erosion. At pH 7.4, the n value was 0.40931, which is below 0.45, denoting a release process dominated by Fickian diffusion.[46]

The knee joints of OA patients are persistently subjected to abnormal mechanical forces. Consequently, the NiN-HDS must demonstrate adequate mechanical stability to retain structural soundness under articular tensile loading, beyond its primary drug-delivery role. Gelatin, however, demonstrates poor structural stability in aqueous environments and fails to provide adequate mechanical support when continuously bathed in synovial fluid. Genipin reacts with the amino groups ($-NH_2$) on the gelatin molecular chains, forming a stable covalent crosslink network that significantly improves the mechanical properties and water stability of the resulting material.[47] As shown in Figure 5A and B, the crosslinked gelatin membrane exhibited approximately double the tensile strength of its uncrosslinked counterpart ($P < 0.05$). Modulating the crosslinking degree allows the mechanical properties of the gelatin membrane to be tuned across a range, thereby better corresponding to the mechanical requirements of OA cartilage. In this study, adjusting the crosslinking degree yielded a gelatin layer with the requisite mechanical properties while preserving some deformability. This crosslinking also altered its degradation profile, enabling the structure to maintain integrity for an extended duration amidst increased synovial fluid and rapid clearance.

Tensile testing of Blank-HDS, CXB-NF-HDS, and NiN-HDS revealed similar fracture strength, elongation at break, and Young's modulus across all samples (Figure 5C–F), indicating that drug loading minimally affected the mechanical properties of NiN-HDS. The Young's modulus of NiN-HDS was 17.239 ± 2.645 MPa, higher than the 0.5–7.5 MPa range for healthy knee cartilage,[48] a stiffness sufficient to bear joint loads, reduce contact stress on the cartilage surface, and potentially delay cartilage degeneration. With an elongation at break of 307.478 ± 32.011%, NiN-HDS demonstrated excellent dynamic deformation capacity, enabling it to accommodate repeated joint motion without fracture. Its fracture

Table 1 Fitting of the pH 6.8 and pH 7.4 in vitro Release Model (n=6)

Formulation	Release Model	pH 6.8		pH 7.4	
		Fitting equation	R^2	Fitting Equation	R^2
CXB-NPs	Zero order	$Q(t)=0.24442t+63.69475$	0.45362	$Q(t)=0.19681t+68.27168$	0.32915
	First order kinetics	$Q(t)=90.16815(1-e^{-0.29327t})$	0.89812	$Q(t)=90.00471(1-e^{-0.37766t})$	0.9112
	Higuchi	$Q(t)=3.97453t^{1/2}+52.51709$	0.65959	$Q(t)=3.33518t^{1/2}+58.40952$	0.53942
	Ritger-Peppas	$Q(t)=48.65028t^{0.14283}$	0.83869	$Q(t)=53.81592t^{0.12023}$	0.75715
CXB-NF-HDS	Zero order	$Q(t)=0.38569t+29.35347$	0.63527	$Q(t)=0.36061t+29.42481$	0.61288
	First order kinetics	$Q(t)=77.20785(1-e^{-0.05941t})$	0.99085	$Q(t)=74.23093(1-e^{-0.0627t})$	0.98658
	Higuchi	$Q(t)=6.02279t^{1/2}+13.30775$	0.83029	$Q(t)=5.6651t^{1/2}+14.20539$	0.81287
	Ritger-Peppas	$Q(t)=16.97268t^{0.32041}$	0.88968	$Q(t)=17.23635t^{0.30921}$	0.879
NiN-HDS	Zero order	$Q(t)=0.38t+14.30201$	0.85622	$Q(t)=0.36898t+17.30743$	0.84298
	First order kinetics	$Q(t)=64.08508(1-e^{-0.02883t})$	0.97598	$Q(t)=64.01718(1-e^{-0.03534t})$	0.97884
	Higuchi	$Q(t)=5.58336t^{1/2}+0.73446$	0.97114	$Q(t)=5.44352t^{1/2}+3.99252$	0.96488
	Ritger-Peppas	$Q(t)=7.03619t^{0.45269}$	0.99054	$Q(t)=8.90658t^{0.40931}$	0.97994

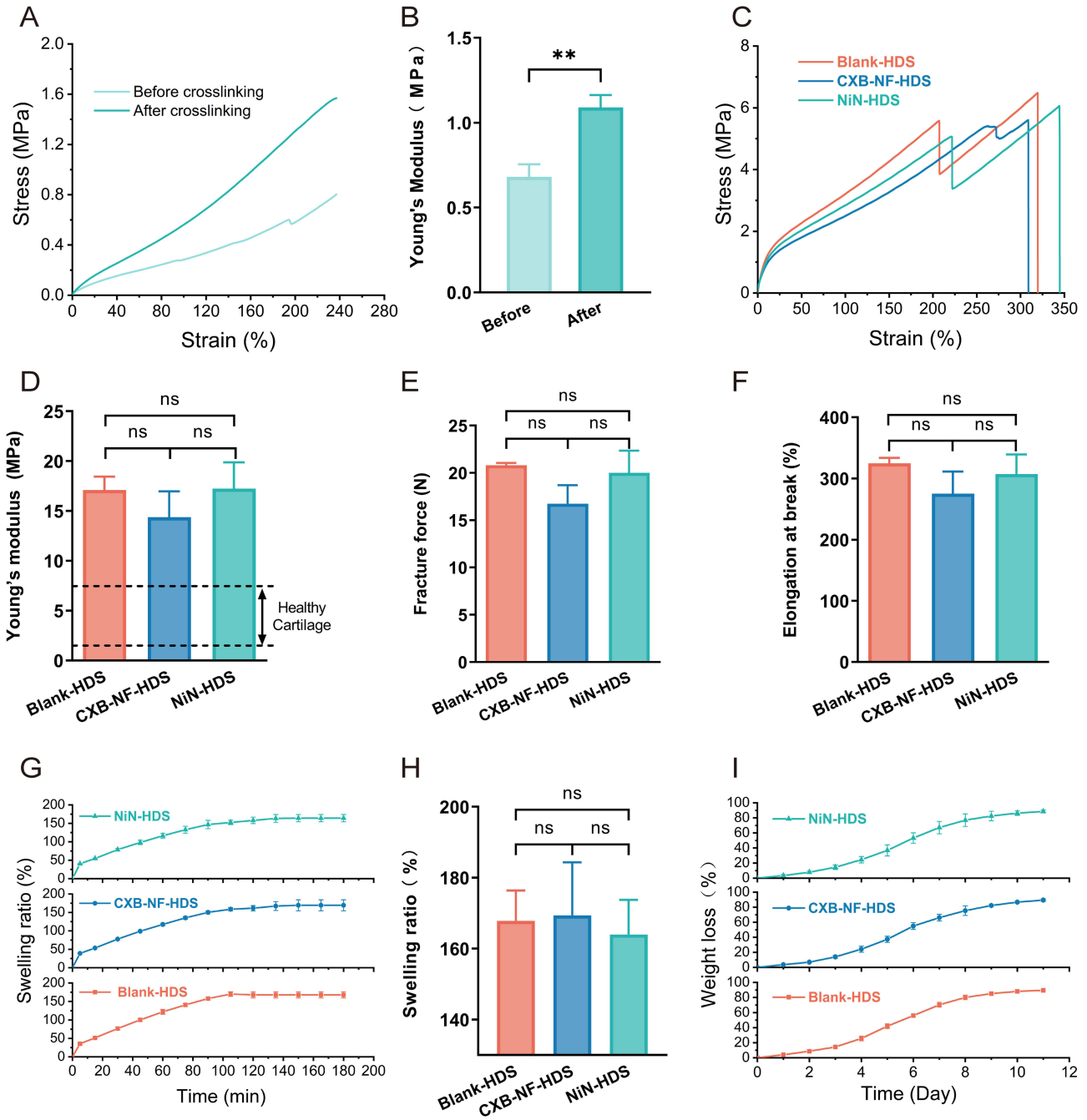

Figure 5 Swelling, degradation, and mechanical properties of different formulations. (**A** and **B**) Stress–strain curves and Young's modulus of the gelatin layer before and after crosslinking. (**C**) Stress–strain curves. (**D**) Young's modulus. (**E**) Elongation at break. (**F**) Fracture force. (**G**) Swelling profiles. (**H**) Equilibrium swelling ratios. (**I**) Degradation profiles. The formulations investigated were Blank-HDS, CXB-NF-HDS, and NiN-HDS. Each value represents the mean ± SD of three experiments. ($^{ns}P > 0.05$; $^{**}P < 0.01$).

strength of 20.02 ± 2.34 N is greater than typical physiological joint loads, ensuring the implant maintains mechanical stability under long-term mechanical stress.

The swelling behavior of Blank-HDS, CXB-NF-HDS, and NiN-HDS is shown in Figure 5G. All three samples rapidly absorbed water and swelled during the initial stage, reaching swelling equilibrium after approximately 150 min. At equilibrium (Figure 5H), the swelling ratios of all groups ranged from 150% to 180% ($P > 0.05$), with NiN-HDS showing a swelling ratio of 163.97 ± 9.76%. Volume expansion within this range is unlikely to significantly affect intra-articular implantation[49] To evaluate biodegradability, the mass loss of NiN-HDS was monitored in phosphate buffer (pH

https://doi.org/10.2147/DDDT.S601447

7.4, 37°C) to analyze its degradation behavior. As shown in Figure 5I, NiN-HDS degraded continuously in vitro for over 10 days, with its degradation rate approaching 88.53 ± 2.03% by day 10.

Therapeutic Efficacy in a Rat OA Model

As shown in Figure 6A, a rat OA model was created via intra-articular injection of sodium iodoacetate to evaluate the efficacy of NiN-HDS in modulating the joint inflammatory microenvironment and promoting cartilage repair. Hind limb grip strength measured on day 28 (Figure 6B) was significantly lower in the model and all treatment groups than in the normal group, exhibiting a continuous decline. Behavioral assessments using the modified Lequesne MG scoring system evaluated knee joint pain, gait, and joint swelling. By day 28, rats injected with MIA exhibited a deteriorated mental state, reduced food intake, weight loss, restricted lower limb joint mobility, and pronounced lameness. Stimulation of the affected area with a cotton swab evoked pain responses, including limb withdrawal, spasms, and mild generalized tremors, yielding scores significantly higher than those in the normal group. These grip-strength and behavioral-scoring results confirmed the successful establishment of the model. Figure 6C presents the post-treatment Lequesne MG scores, which were significantly lower in all treatment groups relative to the model group. Macroscopic morphological changes in the knee joint cartilage on day 35 are shown in Figure 6H. The normal group exhibited smooth, uniformly colored cartilage with clear borders. In contrast, the model and sham surgery groups displayed rough, ulcerated surfaces with cartilage defects, shedding, exposed subchondral bone, osteophyte formation, and increased joint effusion. This CXB group showed localized cartilage whitening and persistent effusion but no large-scale cartilage loss. In contrast, the NiN-HDS group showed a marked reduction in cartilage defects, with no large-scale loss or subchondral bone exposure, resulting in a cartilage surface morphology closer to that of the normal group. The Pelletier scoring results (Figure 6D) showed significant differences in both the CXB group ($P < 0.05$) and the NiN-HDS group ($P < 0.001$) compared with the model group. Moreover, the NiN-HDS group exhibited significantly greater cartilage protection than the positive control group ($P < 0.05$).

H&E staining (Figure 6I) further verified these alterations. In the normal group, the cartilage exhibited an intact structure, normal thickness, a smooth surface, and a well-organized, stratified chondrocyte arrangement. Both the model and sham surgery groups displayed reduced cartilage thickness, structural disruption, and chondrocyte nuclei with diminished staining indicative of cell loss or necrosis, alongside inflammatory cell infiltration and subchondral bone vascular invasion. Relative to the normal group, the CXB group demonstrated a modest increase in cartilage thickness, a relatively preserved structural wholeness, and a higher chondrocyte count. In the NiN-HDS treatment group, cartilage thickness was normal. Compared with the model group, this group showed improved joint structural unity, a greater number of densely packed chondrocytes, and clearly visible boundaries between the calcified and radial layers. Safranin O-fast green staining (Figure 6I) revealed an intact cartilage structure with uniform staining and a well-defined boundary between hyaline and calcified cartilage, presenting a comb-like appearance, in the normal group. In the model and sham surgery groups, the damaged cartilage stained poorly, with disorganized cells and near-total loss of structure. The CXB group exhibited partial structural restoration, a clear calcified layer boundary, and lighter staining, showing a degree of therapeutic benefit. The NiN-HDS treatment group displayed a nearly intact cartilage structure with routine staining, a distinct calcified layer boundary, and pronounced therapeutic effects. Based on the Mankin score results (Figure 6E), the CXB group differed significantly from the model group ($P < 0.01$). In contrast, the therapeutic effect of the NiN-HDS group was even more substantial ($P < 0.001$). These data indicate that the NiN-HDS treatment group yielded the best therapeutic outcome.

Abnormal mechanical loading activates mechanosensitive signaling pathways in chondrocytes, resulting in excessive MMP expression.[50] Mechanical stress concurrently promotes the production of inflammatory mediators, consequently amplifying local inflammatory responses. The key pro-inflammatory cytokine IL-1β, which drives inflammatory cascades and catabolic responses,[51] upregulates degrading enzymes such as MMPs while inhibiting matrix synthesis. As a core protease responsible for cartilage collagen degradation, MMP-13 directly degrades ECM components, including type II collagen, accelerating ECM destruction and weakening cartilage's capacity to withstand abnormal loads.[52] This process ultimately establishes a vicious cycle of mechanical injury, inflammatory response, and

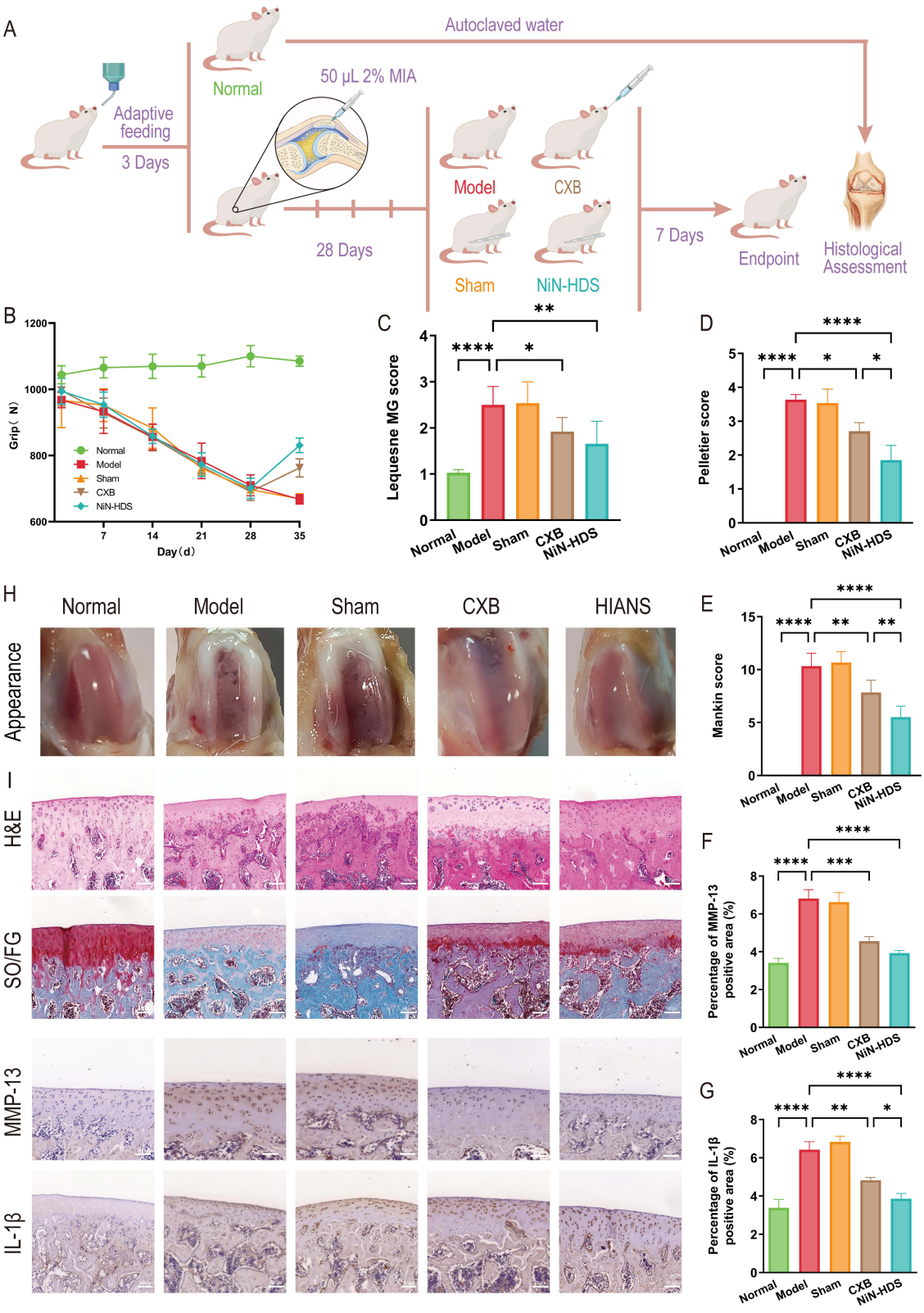

Figure 6 Efficacy of celecoxib in different dosage forms in the OA rat model. (**A**) Schematic of OA model establishment and group-based drug administration. (**B**) Changes in hind limb grip strength of rats during the experiment. (**C**) Lequesne MG scores of rats at the endpoint. (**D**) Pelletier scores of articular cartilage in rats at the endpoint. (**E**) Mankin scores of articular cartilage in rats. (**F**) Quantitative analysis of the relative area coverage of MMP-13. (**G**) Quantitative analysis of the relative area coverage of IL-1β. (**H**) Gross appearance of rat articular cartilage. (**I**) Histological staining (hematoxylin and eosin, safranine O–fast green), and immunohistochemical analysis (IL-1β and MMP-13) of rat articular cartilage. n=8 per group. Significant differences analysis in all groups compared with the model group (*$P < 0.05$; **$P < 0.01$; ***$P < 0.001$; ****$P < 0.0001$).

https://doi.org/10.2147/DDDT.S601447

tissue degeneration.[53] Immunohistochemical staining for MMP-13 and IL-1β (Figure 6F and G) demonstrated a significant upregulation of MMP-13 in the model group ($P < 0.001$). This exacerbated ECM degradation, leading to cartilage erosion and even subchondral bone exposure, as evidenced by poor staining and cartilage rupture in Figure 6I. In contrast, CXB intervention effectively suppressed MMP-13 expression, with the NiN-HDS group exhibiting the most pronounced effect. Furthermore, IL-1β expression was significantly higher in the model group than in the normal group ($P < 0.001$). In contrast, all treatment groups downregulated IL-1β expression to varying degrees, with the NiN-HDS group again showing the greatest reduction. This outcome may be attributed to the structural separation of drug-delivery and mechanical-support functions in NiN-HDS, which synergistically optimizes drug release and mechanical compatibility to balance sustained anti-inflammatory delivery with local mechanical support.

Integrated Structural Advantages of the NiN-HDS

The nanofiber membrane features a "Nano-in-Nano" structure, in which the inner CXB-NPs enable high drug loading and sustained release, maintaining a relatively stable local drug concentration despite the rapid turnover of synovial fluid in the joint cavity. The outer electrospun nanofiber membrane is highly porous and hydrophilic, which promotes the penetration of the release medium and establishes continuous diffusion pathways; this transforms drug release from simple diffusion into a multi-layer process co-regulated by the nanoparticles and the fiber network, thereby preventing an initial burst release. The electrospun membrane's high specific surface area provides abundant attachment sites, and its ECM-like morphology mimics the natural extracellular matrix, together creating favorable conditions for cell adhesion and growth. Furthermore, the crosslinked gelatin layer possesses deformability and mechanical strength, allowing it to buffer abnormal loads and interfacial friction during joint movement and mitigate cartilage damage from sustained mechanical stress. While injectable hydrogel drug delivery systems are widely used for intra-articular delivery and can improve drug retention and joint lubrication, their structure is vulnerable to frequent compression, shear, and wear in the dynamic joint environment.[51,54] Moreover, when drug release and mechanical support rely on the identical structure, a trade-off between diffusion performance and mechanical stability frequently arises. In contrast, NiN-HDS partially overcomes the design constraints imposed by multifunctional coupling through the structural separation of the drug delivery layer and the mechanical support layer. This decoupled architecture allows both components to be independently optimized while achieving synergistic improvements in drug delivery efficacy and mechanical compatibility, two features that are often challenging to reconcile in conventional hydrogels or microspheres.[55] Collectively, NiN-HDS produces synergistic effects on anti-inflammatory drug delivery, and mechanical support, helping to disrupt the pathological cycle of mechanical damage and inflammation in OA progression. Although this study shows that NiN-HDS provides benefits in anti-inflammatory release and mechanical compatibility, certain limitations continue. The work primarily employed a small-animal OA model, whose joint mechanical environment differs from that in the clinical condition. Its durable stability and treatment effectiveness require additional confirmation in large-animal models that better replicate clinical loading conditions.[56] In recent years, local biomaterial systems for OA treatment have increasingly focused on biophysical regulatory strategies, such as mechanoresponsive, electrical stimulation, and ultrasound-responsive approaches.[57,58] Unlike these studies, which primarily emphasize biophysical stimulation or pain modulation, the present study focuses on achieving synergistic optimization of anti-inflammatory drug delivery and local mechanical support through a hierarchical structure. In the future, the layered architecture of NiN-HDS could be further integrated with stimuli-responsive or multidrug delivery strategies to enhance comprehensive intervention in the complex pathological processes of OA.

Conclusion

In this study, a celecoxib-loaded "Nano-in-Nano" hierarchical delivery system (NiN-HDS) was successfully developed, achieving synergistic optimization of drug delivery and mechanical support through a layered design. In vitro experiments demonstrated sustained drug release for over seven days under OA-mimetic conditions, effectively minimizing the initial burst release and maintaining nanoparticle stability. Mechanical testing indicated that NiN-HDS possesses sufficient Young's modulus to share joint load and accommodate dynamic motion without structural failure. In vivo evaluation in a rat osteoarthritis model showed that NiN-HDS significantly reduced cartilage degeneration and suppressed local inflammation, confirming its

therapeutic potential. The hierarchical "nanoparticle–nanofiber–gelatin" structure enables functional separation and cooperative optimization, ensuring both controlled drug release and mechanical compatibility. Collectively, these findings indicate that NiN-HDS represents a promising implantable intra-articular platform for the localized treatment of osteoarthritis and other weight-bearing joint diseases.

Data Sharing Statement

Data supporting the findings of this study are available upon reasonable request to the corresponding author.

Ethics Approval

The experiment was approved prior to commencement by the Guangdong Pharmaceutical University Institutional Animal Ethics and Use Committee, which ensured that animal experiments were in compliance with the National Institutes of Health's Guidelines for the Ethics and Use of Laboratory Animals.(Approval Code: gdpulacspf2022160).

Consent for Publication

The authors declare that they have no known competing financial interests or personal relationships that could have appeared to influence the work reported in this paper.

Author Contributions

All authors made a significant contribution to the work reported, whether in conception, study design, execution, acquisition of data, analysis or interpretation or in all of these areas; took part in drafting, revising or critically reviewing the manuscript; gave final approval of the version to be submitted; agreed on the journal to which the manuscript was submitted; and agreed to be accountable for all aspects of the work.

Funding

This work was supported by the Natural Science Foundation of Guangdong Province (Grant No. 2023A1515010470).

Disclosure

The authors report no conflicts of interest in this work.

References

1. Glyn-Jones S, Palmer AJR, Agricola R, et al. Osteoarthritis. *Lancet*. 2015;386(9991):376–387. doi:10.1016/S0140-6736(14)60802-3
2. Jiang Y. Osteoarthritis year in review 2021: biology. *Osteoarthritis Cartilage*. 2022;30(2):207–215. doi:10.1016/j.joca.2021.11.009
3. GBD 2021 Osteoarthritis Collaborators. Global, regional, and national burden of osteoarthritis, 1990-2020 and projections to 2050: a systematic analysis for the global burden of disease study 2021. *Lancet Rheumatol*. 2023;5(9):e508–e522. doi:10.1016/S2665-9913(23)00163-7
4. Batarfi WA, Yunus MHM, Hamid AA, Maarof M, Abdul Rani R. Breaking down osteoarthritis: exploring inflammatory and mechanical signaling pathways. *Life*. 2025;15(8):1238. doi:10.3390/life15081238
5. Nieuwstraten J, Riester R, Hofmann UK, Guilak F, Danalache M. Matrix metalloproteinases accelerate pericellular matrix breakdown and disrupt mechanotransduction in osteoarthritis. *Acta Biomater*. 2025;195:73–82. doi:10.1016/j.actbio.2025.02.034
6. Jiang T, Su S, Tian R, et al. Immunoregulatory orchestrations in osteoarthritis and mesenchymal stromal cells for therapy. *J Orthop Transl*. 2025;55:38–54. doi:10.1016/j.jot.2025.08.009
7. Richard MJ, Driban JB, McAlindon TE. Pharmaceutical treatment of osteoarthritis. *Osteoarthritis Cartilage*. 2023;31(4):458–466. doi:10.1016/j.joca.2022.11.005
8. Harirforoosh S, Asghar W, Jamali F. Adverse effects of nonsteroidal antiinflammatory drugs: an update of gastrointestinal, cardiovascular and renal complications. *J Pharm Pharm Sci*. 2013;16(5):821–847. doi:10.18433/J3VW2F
9. Maroudas A. Transport of solutes through cartilage: permeability to large molecules. *J Anat*. 1976;122(Pt 2):335–347.
10. Kavanaugh TE, Werfel TA, Cho H, Hasty KA, Duvall CL. Particle-based technologies for osteoarthritis detection and therapy. *Drug Deliv Transl Res*. 2016;6(2):132–147. doi:10.1007/s13346-015-0234-2
11. Mei H, Sha C, Lv Q, et al. Multifunctional polymeric nanocapsules with enhanced cartilage penetration and retention for osteoarthritis treatment. *J Control Release*. 2024;374:466–477. doi:10.1016/j.jconrel.2024.08.031
12. Chen Q, Jin Y, Chen T, et al. Injectable nanocomposite hydrogels with enhanced lubrication and antioxidant properties for the treatment of osteoarthritis. *Mater Today Bio*. 2024;25:100993. doi:10.1016/j.mtbio.2024.100993
13. Spitters TWGM, Stamatialis D, Petit A, de Leeuw MGW, Karperien M. In vitro evaluation of small molecule delivery into articular cartilage: effect of synovial clearance and compressive load. *Assay Drug Dev Technol*. 2019;17(4):191–200. doi:10.1089/adt.2018.907

14. Meng H, Quan Q, Yuan X, et al. Diffusion of neutral solutes within human osteoarthritic cartilage: effect of loading patterns. *J Orthop Transl*. 2020;22:58–66. doi:10.1016/j.jot.2019.10.013
15. Belluzzi E, Todros S, Pozzuoli A, et al. Human cartilage biomechanics: experimental and theoretical approaches towards the identification of mechanical properties in healthy and osteoarthritic conditions. *Processes*. 2023;11(4):1014. doi:10.3390/pr11041014
16. Wang L, Wang P, Liu Y, et al. The effect of different factors on Poly(lactic-co-glycolic acid) nanoparticle properties and drug release behaviors when co-loaded with hydrophilic and hydrophobic drugs. *Polymers*. 2024;16(7):865. doi:10.3390/polym16070865
17. Shetty K, Bhandari A, Yadav KS. Nanoparticles incorporated in nanofibers using electrospinning: a novel nano-in-nano delivery system. *J Control Release*. 2022;350:421–434. doi:10.1016/j.jconrel.2022.08.035
18. Shibata T, Yoshimura N, Kobayashi A, et al. Emulsion-electrospun polyvinyl alcohol nanofibers as a solid dispersion system to improve solubility and control the release of probucol, a poorly water-soluble drug. *J Drug Delivery Sci Technol*. 2022;67:102953. doi:10.1016/j.jddst.2021.102953
19. Chen S, Li R, Li X, Xie J. Electrospinning: an enabling nanotechnology platform for drug delivery and regenerative medicine. *Adv Drug Deliv Rev*. 2018;132:188–213. doi:10.1016/j.addr.2018.05.001
20. Walejewska E, Melchels FPW, Paradiso A, et al. Tuning physical properties of GelMA hydrogels through microarchitecture for engineering osteoid tissue. *Biomacromolecules*. 2024;25(1):188–199. doi:10.1021/acs.biomac.3c00909
21. Chu K, Zhu Y, Lu G, et al. Formation of hydrophilic nanofibers from nanostructural design in the co-encapsulation of celecoxib through electrospinning. *Pharmaceutics*. 2023;15(3):730. doi:10.3390/pharmaceutics15030730
22. Brenner S, Horne RW. A negative staining method for high resolution electron microscopy of viruses. *Biochim Biophys Acta*. 1959;34:103–110. doi:10.1016/0006-3002(59)90237-9
23. Alassaif FR, Alassaif ER, Kaushik AK, Dhanapal J. Enhanced anti-proliferative effect of carboplatin in ovarian cancer cells exploiting chitosan-poly (lactic glycolic acid) nanoparticles. *Recent Pat Nanotechnol*. 2023;17(1):74–82. doi:10.2174/1872210516666220111160341
24. Asal HA, Shoueir KR, El-Hagrasy MA, Toson EA. Controlled synthesis of in-situ gold nanoparticles onto chitosan functionalized PLGA nanoparticles for oral insulin delivery. *Int J Biol Macromol*. 2022;209(Pt B):2188–2196. doi:10.1016/j.ijbiomac.2022.04.200
25. Drzeżdżon J, Jacewicz D, Sielicka A, Chmurzyński L. Characterization of polymers based on differential scanning calorimetry based techniques. *TrAC Trends in Analytical Chemistry*. 2019;110:51–56. doi:10.1016/j.trac.2018.10.037
26. Brittain HG. X-ray diffraction of pharmaceutical materials. *Profiles Drug Subst Excip Relat Methodol*. 2003;30:271–319. doi:10.1016/S0099-5428(03)30010-3
27. Song Y, Cong Y, Wang B, Zhang N. Applications of fourier transform infrared spectroscopy to pharmaceutical preparations. *Expert Opin Drug Delivery*. 2020;17(4):551–571. doi:10.1080/17425247.2020.1737671
28. Pan X, Li R, Li W, et al. Silk fibroin hydrogel adhesive enables sealed-tight reconstruction of meniscus tears. *Nat Commun*. 2024;15(1):2651. doi:10.1038/s41467-024-47029-6
29. Yu M, Yuan W, Li D, Schwendeman A, Schwendeman SP. Predicting drug release kinetics from nanocarriers inside dialysis bags. *J Control Release*. 2019;315:23–30. doi:10.1016/j.jconrel.2019.09.016
30. Pati F, Adhikari B, Dhara S. Development of chitosan-tripolyphosphate non-woven fibrous scaffolds for tissue engineering application. *J Mater Sci Mater Med*. 2012;23(4):1085–1096. doi:10.1007/s10856-012-4559-9
31. Shi T, Liu Y, Wang D, et al. Spatially engineering tri-layer nanofiber dressings featuring asymmetric wettability for wound healing. *Nano Mater Sci*. 2024;6(5):611–624. doi:10.1016/j.nanoms.2024.01.008
32. Rashid TU, Gorga RE, Krause WE. Mechanical properties of electrospun fibers—a critical review. *Adv Eng Mater*. 2021;23(9):2100153. doi:10.1002/adem.202100153
33. Pitcher T, Sousa-Valente J, Malcangio M. The monoiodoacetate model of osteoarthritis pain in the mouse. *J Vis Exp*. 2016;(111):53746. doi:10.3791/53746
34. Mastbergen SC, Lafeber FPJG, Bijlsma JWJ. Selective COX-2 inhibition prevents proinflammatory cytokine-induced cartilage damage. *Rheumatology*. 2002;41(7):801–808. doi:10.1093/rheumatology/41.7.801
35. Faucher M, Poiraudeau S, Lefevre-Colau MM, et al. Algo-functional assessment of knee osteoarthritis: comparison of the test-retest reliability and construct validity of the WOMAC and lequesne indexes. *Osteoarthritis Cartilage*. 2002;10(8):602–610. doi:10.1053/joca.2002.0533
36. Gerwin N, Bendele AM, Glasson S, Carlson CS. The OARSI histopathology initiative - recommendations for histological assessments of osteoarthritis in the rat. *Osteoarthritis Cartilage*. 2010;18(Suppl 3):S24–S34. doi:10.1016/j.joca.2010.05.030
37. Afara I, Prasadam I, Crawford R, Xiao Y, Oloyede A. Non-destructive evaluation of articular cartilage defects using near-infrared (NIR) spectroscopy in osteoarthritic rat models and its direct relation to mankin score. *Osteoarthritis Cartilage*. 2012;20(11):1367–1373. doi:10.1016/j.joca.2012.07.007
38. Blanco E, Shen H, Ferrari M. Principles of nanoparticle design for overcoming biological barriers to drug delivery. *Nat Biotechnol*. 2015;33(9):941–951. doi:10.1038/nbt.3330
39. Öztürk K, Kaplan M, Çalış S. Effects of nanoparticle size, shape, and zeta potential on drug delivery. *Int J Pharm*. 2024;666:124799. doi:10.1016/j.ijpharm.2024.124799
40. Arslan A, Yet B, Nemutlu E, et al. Celecoxib nanoformulations with enhanced solubility, dissolution rate, and oral bioavailability: experimental approaches over In vitro/In vivo evaluation. *Pharmaceutics*. 2023;15(2):363. doi:10.3390/pharmaceutics15020363
41. Pandya V, Patel D, Jayvadan P, Patel R. Formulation, characterization, and optimization of fast-dissolve tablets containing celecoxib solid dispersion. *Dissolution Technol*. 2009;16(4):22–27. doi:10.14227/DT160409P22
42. Chawla G, Gupta P, Thilagavathi R, Chakraborti AK, Bansal AK. Characterization of solid-state forms of celecoxib. *Eur J Pharm Sci*. 2003;20(3):305–317. doi:10.1016/s0928-0987(03)00201-x
43. He J, Han Y, Xu G, et al. Preparation and evaluation of celecoxib nanosuspensions for bioavailability enhancement. *RSC Adv*. 2017;7(22):13053–13064. doi:10.1039/C6RA28676C
44. Wu H, Xiao D, Lu J, et al. Preparation and properties of biocomposite films based on poly(vinyl alcohol) incorporated with eggshell powder as a biological filler. *J Polym Environ*. 2020;28(7):2020–2028. doi:10.1007/s10924-020-01747-2
45. Yoo J, Won YY. Phenomenology of the initial burst release of drugs from PLGA microparticles. *ACS Biomater Sci Eng*. 2020;6(11):6053–6062. doi:10.1021/acsbiomaterials.0c01228

46. Wu IY, Bala S, Škalko-Basnet N, Di Cagno MP. Interpreting non-linear drug diffusion data: utilizing korsmeyer-peppas model to study drug release from liposomes. *Eur J Pharm Sci*. 2019;138:105026. doi:10.1016/j.ejps.2019.105026
47. Oryan A, Kamali A, Moshiri A, Baharvand H, Daemi H. Chemical crosslinking of biopolymeric scaffolds: current knowledge and future directions of crosslinked engineered bone scaffolds. *Int J Biol Macromolecules*. 2018;107:678–688. doi:10.1016/j.ijbiomac.2017.08.184
48. Niu H, Liu C, Li A, et al. Relationship between triphasic mechanical properties of articular cartilage and osteoarthritic grade. *Sci China Life Sci*. 2012;55(5):444–451. doi:10.1007/s11427-012-4326-7
49. Shen C, Wang J, Li G, et al. Boosting cartilage repair with silk fibroin-DNA hydrogel-based cartilage organoid precursor. *Bioact Mater*. 2024;35:429–444. doi:10.1016/j.bioactmat.2024.02.016
50. Tetsunaga T, Nishida K, Furumatsu T, et al. Regulation of mechanical stress-induced MMP-13 and ADAMTS-5 expression by RUNX-2 transcriptional factor in SW1353 chondrocyte-like cells. *Osteoarthritis Cartilage*. 2011;19(2):222–232. doi:10.1016/j.joca.2010.11.004
51. Han Y, Yang J, Zhao W, et al. Biomimetic injectable hydrogel microspheres with enhanced lubrication and controllable drug release for the treatment of osteoarthritis. *Bioact Mater*. 2021;6(10):3596–3607. doi:10.1016/j.bioactmat.2021.03.022
52. Diaz-Rodriguez P, Mariño C, Vázquez JA, Caeiro-Rey JR, Landin M. Targeting joint inflammation for osteoarthritis management through stimulus-sensitive hyaluronic acid based intra-articular hydrogels. *Mater Sci Eng*. 2021;128:112254. doi:10.1016/j.msec.2021.112254
53. He Y, Sun M, Wang J, et al. Chondroitin sulfate microspheres anchored with drug-loaded liposomes play a dual antioxidant role in the treatment of osteoarthritis. *Acta Biomater*. 2022;151:512–527. doi:10.1016/j.actbio.2022.07.052
54. Li G, Liu S, Chen Y, et al. An injectable liposome-anchored teriparatide incorporated gallic acid-grafted gelatin hydrogel for osteoarthritis treatment. *Nat Commun*. 2023;14(1):3159. doi:10.1038/s41467-023-38597-0
55. Wang F, Han X, Han Z, et al. Slide-ring structured stress-electric coupling hydrogel microspheres for low-loss transduction between tissues. *Adv Mater*. 2025;37(7):e2413156. doi:10.1002/adma.202413156
56. Pang L, Xiang L, Chen G, Cui W. In-situ hydrogen-generating injectable short fibers for osteoarthritis treatment by alleviating oxidative stress. *Acta Biomater*. 2024;188:406–419. doi:10.1016/j.actbio.2024.09.008
57. Han Z, Wang F, Xiong W, et al. Precise cell type electrical stimulation therapy via force-electric hydrogel microspheres for cartilage healing. *Adv Mater*. 2025;37(7):e2414555. doi:10.1002/adma.202414555
58. Li X, Wang F, Zhang X, et al. Ultrasound-responsive piezoelectric analgesic microspheres alleviate osteoarthritis pain. *J Control Release*. 2025;385:114049. doi:10.1016/j.jconrel.2025.114049